Soft Matter

Cite this: *Soft Matter*, 2012, **8**, 4767

www.rsc.org/softmatter

PAPER

Phase behaviour and Janus hierarchical supramolecular structures based on asymmetric tapered bisamide†

Hao-Jan Sun,[a] Chien-Lung Wang,[ab] I-Fan Hsieh,[a] Chih-Hao Hsu,[a] Ryan M. Van Horn,[a] Chi-Chun Tsai,[a] Kwang-Un Jeong,[c] Bernard Lotz[d] and Stephen Z. D. Cheng*[a]

Received 9th December 2011, Accepted 14th February 2012
DOI: 10.1039/c2sm07332c

A precisely defined molecular Janus compound based on asymmetric tapered 1,4-bis[3,4,5-tris(alkan-1-yloxy)benzamido] benzene bisamide (abbreviated as $C_{22}PhBAEO_3$) was designed and synthesized, and its phase behavior was fully investigated. The $C_{22}PhBAEO_3$ compound possesses a rigid core with three aromatic rings connected with amide bonds which possess the ability to form hydrogen (H) bonds. Three hydrophobic alkyl flexible tails and three hydrophilic flexible methyl terminated triethylene glycol tails are located at the other end. Major phase transitions and their origins in $C_{22}PhBAEO_3$ were studied *via* DSC and 1D WAXD techniques. Its hierarchical supramolecular crystal structure was further identified through combined techniques of 2D WAXD and SAXS as well as SAED. Results based on computer simulations confirmed the structure determination. It was found that the $C_{22}PhBAEO_3$ possesses three phases through various thermal treatments including a micro-phase separated columnar liquid crystal (*col.*) phase, a metastable *crystal I* phase and a stable *crystal II* phase. Among them, the *crystal II* phase showed that the columnar structure possesses 3D inter-column order and highly crystalline alkyl tails with a long-range overall orientational order. Four $C_{22}PhBAEO_3$ molecules self-assembled into a phase-separated disc with an ellipsoidal shape having a C_2 symmetry along the disc normal. These discs then stacked on top of each other to generate a 1D asymmetric column through H-bonding, and further packed into a 3D long-range ordered monoclinic lattice. The unit cell parameters of this lattice were determined to be $a = 5.08$ nm, $b = 2.41$ nm, $c = 0.98$ nm, $\alpha = 90°$, $\beta = 90°$, and $\gamma = 70.5°$. The alkyl chain tails crystallize within the hydrophobic layers and possess a relatively fixed orientation with respect to the column packing due to the selective interactions based on the hydrophobic/hydrophilic microphase separation. Both phase behaviour and unit cell structure showed significant difference compared with the symmetrically tapered counterparts. The results provided a new approach of fine-tuning not only in the Janus supramolecular structures but also in the formation pathway of the self-assembling process in order to meet the specific requirements for optical and biological applications.

Introduction

Since the concept of "Janus grains" was introduced in de Gennes' Nobel lecture two decades ago,[1] Janus particles have received extensive attention over the last few decades. They are named after the double-faced Roman god Janus, a representative of dichotomy. In material science, particles that have special asymmetric architecture of two distinct sides or interfaces with different chemical compositions or polarities are named Janus particles. They were found to be both surface active and amphiphilic.[2,3] The non-centrosymmetric (an inversion center operation is absent at the geometric center) character makes them capable of forming complex hierarchical structures showing desired properties for applications such as bio-chemical sensors,[4–10] self-motile particles,[11,12] and interface stabilizers.[3,13,14] Several review articles have summarized the synthetic strategies

[a]*Department of Polymer Science, College of Polymer Science and Polymer Engineering, The University of Akron, Akron, OH, 44325, USA. E-mail: scheng@uakron.edu*
[b]*Department of Applied Chemistry, National Chiao Tung University, 1001 Ta Hsueh Road, Hsinchu, Taiwan 300, ROC*
[c]*Polymer Bin Fusion Research Center, Department of Polymer Nano-Science and Technology, Chonbuk National University, Jeonju, Jeonbuk 561-756, Korea*
[d]*Institut Charles Sadron, 23, Rue du Loess, Strasbourg 67034, France*

† Electronic supplementary information (ESI) available: Fig. S1–S12 include synthetic route, ^{1}H NMR spectrum, ^{13}C NMR spectrum, MALDI-TOF mass spectrum, FT-IR spectrum, TGA diagram, supporting DSC and ED data, ED fiber pattern, disc formation mechanism, and POM morphology of two crystal phases. See DOI: 10.1039/c2sm07332c

and organization pathways as well as potential applications of the Janus entities.[15–19] In general, Janus entities can be derived from inorganic materials, colloidal particles, polymers, liquid crystalline compounds, and supramolecular assemblies. They can be divided into several common classes such as spheres (0D), cylinders (1D), and discs (2D), according to their architectures and dimensionalities. Other architectures including snowman or dumbbell-like, hamburger, and raspberry-like were also reported.[20–22] The lack of centrosymmetry is a common feature to all of these particles and has become the major challenge in their preparation. Syntheses toward molecules with Janus features often require that symmetry breaking of the underlining building blocks takes place first. In order to ensure the formation of 3D long-range ordered structures, molecular Janus entities with high uniformity and molecular precision have been required as reported, including amphiphilic dendrimers,[23,24] colloidal photonic crystals,[25] unimolecular micelles of block copolymers,[10] and polymer brushes.[26,27] However, the demands of sophisticated synthesis techniques and non-trivial purifications have made commercially driven applications less practical. In addition, molecular Janus entities often lack volume- or shape-persistence due to their flexible conformations. On the other hand, facile synthetic routes or self-assembly procedures such as microfluidic co-flow synthesis,[10,28] Pickering emulsion,[29] electrospinning with a bi-phasic nozzle,[30] homopolymer blends,[31] and block copolymer self-assembly in bulk state[32–34] can produce larger quantities of asymmetrical particles; yet, size distribution and composition uniformity are often not guaranteed. Furthermore, engineering approaches such as microfluidic devices[10,35] and pre-patterned templates[36,37] are usually required for those particles to access larger scale Janus structures. Therefore, precisely defined molecular Janus entities obtained through simple preparation procedures that can self-assemble into 3D long-range ordered hierarchical structures with volume- and shape-persistent features are of great interest to develop. In our view, molecular Janus compounds, which readily scale-up and self-assemble into highly ordered supramolecular structures, are closer to this goal.

Supramolecular architectures are considered to be chemistry beyond molecules. Instead of connecting building blocks by covalent bonds, the long-range ordered supramolecular structures are constructed by intermolecular physical interactions such as hydrogen (H)-bonding, electrostatic (ion–ion, ion–dipole, and dipole–dipole) interactions, π–π stacking interactions, van der Waals interactions, hydrophobic–hydrophilic phase separations, and others. Recently, we reported our effort toward self-assembled, hierarchical supramolecular structures in the bulk through the design and synthesis of polyhedral oligomeric silsesquioxane (POSS), [60]fullerene (C_{60}), and porphyrin based molecular Janus particles.[38–40] These dumbbell shaped Janus particles were effectively synthesized by thiol–ene click chemistry and their hierarchical architectures consisting of bilayered structures further organized into 3D orthorhombic lattice within layers were reported.

Holding on to the same principles, our attention has been extended to H-bonding induced columnar supramolecular structures. H-bonding assisted structures have thrived in a dynamic research field due to the moderate bonding energy, reversibility, selectivity and directionality of H-bonding.[41–43] Previously, we have also reported a discotic liquid crystal phase formed by a series of symmetric tapered bisamides (abbreviated as C_nPhBA, where n is the number of carbon atoms in each tail, $n = 6$, 8, 10, 12, 14, and 16) having three alkyl chain tails at each end of the three aromatic ring cores.[44–46] A similar molecular architecture has also been reported by Ungar *et al.*[47] From our previous results, four C_nPhBA were found to generate a disc-like building block through the intermolecular H-bonding, and the supramolecular discs then further assembled into two oblique columnar phases in response to the environment temperature. With these experiences, we would like to investigate which structures and phase behaviours are altered if the symmetry of the bisamide building molecules is lost and the Janus feature is introduced.

In this respect, a series of asymmetrically tapered bisamides (C_MPhBAEO_N) were designed and synthesized by Steglich esterification. The asymmetric bisamide has a rigid core of 1,2-bis [3,4,5-tris(alkan-1-yloxy) benzamido] benzene in the middle, carbon hydrophobic alkyl chain tails with M carbon numbers at one end, and hydrophilic methyl terminated ethylene glycol (EO) tails with N repeat units at the other end. In this article, we chose to report one compound in this series of which $M = 22$ and $N = 3$ (C_{22}PhBAEO_3). The core possesses a rigid plane that consists of three phenylenes connected with amide bonds. In addition to intermolecular H-bonding interactions and core–tail microphase separation force, hydrophilic/hydrophobic microphase separation of the tails has been added to this system (Scheme 1). Thermodynamic properties of the phase transitions in C_{22}PhBAEO_3 were studied by differential scanning calorimetry (DSC) experiments. The phase structures were identified by wide angle X-ray diffraction (WAXD), small angle X-ray scattering (SAXS), and selected area electron diffraction (SAED) experiments. Molecular conformations and packing schemes were obtained by structure analysis and supported by computer simulations. The phase morphologies were also investigated by transmission electron microscopy (TEM). It has been found that

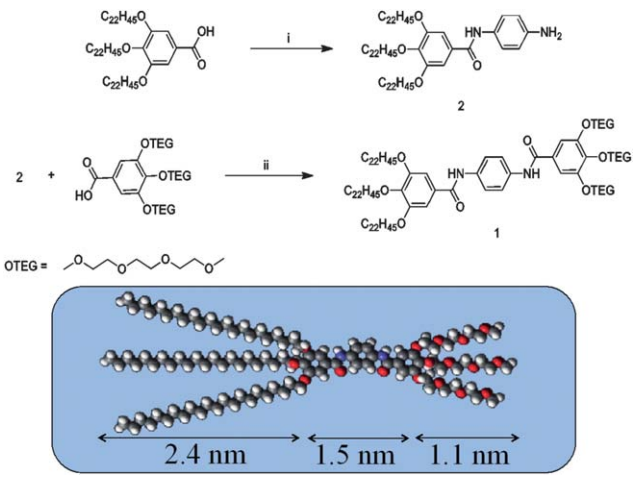

Scheme 1 A brief synthetic route of C_{22}PhBAEO_3 (**1**) is shown. *Reagents and conditions*: (i) 1,4-phenylenediamine, *N*,*N*′-diisopropylcarbodiimide (DIPC), 4-(dimethylamino) pyridinium toluene-*p*-sulfonate (DPTS), THF/CH_2Cl_2 = 1/4, 25 °C; (ii) *N*-(3-dimethylaminopropyl)-*N*′-ethyl-carbodiimide hydrochloride (EDC·HCl), 1-hydroxy-benzotriazole (HOBT), CH_2Cl_2, 25 °C.

four $C_{22}PhBAEO_3$ Janus molecules self-assemble into a 2D phase-separated ellipsoid disc that is formed by the intermolecular H-bonding between the cores. These discs are then further stacked into a supramolecular asymmetric column and further self-organized into a 3D monoclinic lattice with a bilayer character that is constructed by phase separated hydrophobic and hydrophilic tails. Therefore, instead of oblique LC columnar phases as found in symmetric bisamides,[44–46] the asymmetric bisamides formed a 3D long-range ordered hierarchical crystalline structure which can be obtained through moderate temperature annealing.

Experimental

Materials

Tetrahydrofuran (THF) and methanol were purchased from Aldrich as reagent grade and used as received. Anhydrous grade CH_2Cl_2 was purchased from Acros. All other reagents were purchased as reagent grade and used without further purification unless otherwise noted. Compounds 3,4,5-tris-docosoxybenzoic acid and methyl-3,4,5-tris(2-(2-(2-hydroxyethoxy)ethoxy)-ethoxy)benzoic acid were synthesized according to the literature.[46,48] Scheme 1 shows the synthetic route of $C_{22}EO_3$Bisamide ($C_{22}PhBAEO_3$, **1**). Detailed preparation procedure and compound characterization data can be found in the ESI†. Computed molecular dimensions by Cerius^2 software in the extended conformation can also be found at the bottom of Scheme 1. The samples were stored in a vacuum desiccator before conducting characterization.

Sample preparation

For DSC experiments, material with a weight of ~3.0 mg was sealed in an aluminium pan. The sample and reference pan weights were kept constant with a precision of ±0.001 mg. The temperature scanning rate was kept constant at 10 °C min^{-1}. The thin film sample for Fourier transform infrared spectroscopy (FT-IR) was prepared by dilute solution casting from a CH_2Cl_2 solution (0.1% w/v) onto a KBr plate. The plate was heated to 120 °C after solvent evaporation to remove previous thermal history.

For 1D WAXD powder measurements, around 30 mg of material was melted on an aluminium plate to form a film with thickness of ~1 mm. The phase transitions and the corresponding structural transformations were monitored by 1D WAXD experiments in the following three thermal processes according to the transition temperatures observed in DSC thermal diagrams. First, the sample was heated to the isotropic (*I*) melt at 110 °C to remove previous thermal histories, and then, the subsequent cooling and heating thermal diagrams were recorded at a scan rate of 10 °C min^{-1}. Second, the sample was heated to the *I* melt and cooled to room temperature. It was reheated to 87 °C and annealed there for 2 hours. The sample was then brought back to room temperature where the 1D WAXD scan was recorded. Finally, the sample was heated to the *I* melt and directly cooled to 90 °C and annealed there for 1 day. The 1D WAXD scan was recorded after the sample returned to room temperature. The samples prepared by the first two thermal cycles were also subjected to SAXS measurements conducted at room temperature.

The 2D WAXD measurements were performed on mechanically sheared samples. A 2 mg sample was placed on a glass slide and heated to 120 °C followed by cooling from the *I* melt. The sample was mechanically sheared with a sharp razor blade at temperature around 75 °C. Then, the film was removed from the glass surface as a free standing film at 30 °C before recording diffraction patterns. The typical sample thickness was ~0.2 mm. After the first set of experiments, the same piece of sample was annealed at 87 °C for 2 hours and then, brought back to room temperature for another set of 2D WAXD experiments. The diffraction patterns were recorded with the beam aligned along three directions: the through, front, and shear directions, respectively (as indicated in Fig. 3a).

To prepare the TEM samples for SAED experiments and morphological investigation, a dilute solution of $C_{22}PhBAEO_3$ was prepared in CH_2Cl_2 (0.02% w/v). The solution was sprayed onto carbon coated copper grids. After solvent evaporation, the copper grids were subject to the identical thermal treatments as the samples prepared for DSC and 1D WAXD experiments.

To study the surface topology of the self-assembled structure in the thin films, the polyethylene surface lamellar decoration (PE-SLD) technique[49,50] was applied to study the surface texture of the supramolecular structures. This technique was widely used in studying fold surface of polymer single crystals.[49–52] In a short description of this method, 0.2 mg of linear HDPE (M_n = 17.3 kg mol^{-1} with PDI = 1.11, Phillips Petroleum Co.) was placed in a tungsten basket in a vacuum evaporator with sample grids inside. The PE molecules degraded into small fragments during heating in the vacuum chamber. The fragments evaporated and deposited onto the sample surface to reveal the surface texture of the self-assembled structure. Each fragment possessed a length of ~20 nm and, thus, the width of the PE rod crystals.

To measure the crystal density, a small amount of crystals (~ 0.5 mg) were collected and placed in a vial filled with water followed by ultrasonication to remove the air bubbles embedded within the sample. The sample then sank to the bottom of the vial due to its higher density compared with water. Potassium iodide (KI) was then added into the solution at ~0.1 g per aliquot to gradually increase the solution density. KI was added at an interval of at least 20 min to ensure that equilibrium within the solution was reached. When the sample was suspended in the middle of the mixed solution, the density of the sample was identical to that of the solution. The solution density was determined by the composition when the sample was suspended.

Equipment and experiments

Various characterization techniques were utilized to identify the chemical structure of the synthesized sample. ^{1}H NMR spectrum analysis was performed on a Varian Gemini 300 NMR at 300 MHz; the spectrum was referenced to the residual proton impurities in $CDCl_3$ at δ 7.27 ppm. ^{13}C NMR spectrum analysis was performed on a Varian Gemini 300 NMR at 75 MHz; the spectrum was referenced to $^{13}CDCl_3$ at δ 77.00 ppm.

Bruker Ultraflex III TOF equipped with a Nd:YAG laser emitting at 355 nm (Bruker Daltonics, Inc., Billerica, MA) was used to carry out the matrix-assisted laser desorption/ionization-time of

flight (MALDI-TOF) measurement. The positive reflector mode was adopted when recording all spectra. Instrument calibration was performed with external standards, poly(methyl methacrylate) and polystyrene, prior to every measurement. Data analysis was performed on the flexAnalysis software package. FT-IR (Digilab Win-IR Pro FTS 3000) equipped with a Bruker heating stage was used to study the hydrogen bonding and molecular chain conformations (results are reported in ESI†).

Differential scanning calorimetry (DSC) experiments were carried out on a Perkin-Elmer PYRIS Diamond differential scanning calorimeter with an Intracooler 2P apparatus. Calibration was performed by using standard materials on both temperature and heat flow scales at various heating and cooling rates (2.5–40 °C min^{-1}). Transition temperatures were determined according to the onset temperatures which were defined as the cross-point of the peak slope and the baseline in the DSC thermal diagrams. The onset temperature was determined on the high-temperature side during cooling and on the low-temperature side during heating. Thermogravimetric measurements were conducted prior to the DSC experiments on a TA TGA Q500 instrument at a 10 °C min^{-1} scan rate under nitrogen atmosphere.

1D WAXD measurements were performed on a Rigaku Multiflex 2 kW Automated Diffractometer equipped with CuK_α radiation ($\lambda = 0.1542$ nm). A hot stage calibrated with a deviation within ±0.5 °C is coupled with the diffractometer for structure phase transition studies as a function of temperature. Sample scanning rate was fixed at 1° min^{-1} within the 2θ range of 1.8–40°. The sample chamber was evacuated before recording the spectrum. 2D-WAXD fiber experiments were carried out on a Rigaku 18 kW rotating anode X-ray generator attached to an R-AXIS-IV image plate system. The mechanically sheared samples were exposed for 40 to 60 minutes to ensure the high quality diffraction patterns. The X-ray beams were monochromatized by graphite crystals. The observed 2θ diffraction positions above 15° were calibrated by silicon crystals with known periodic 2θ diffractions, and silver behenate was used for calibrating diffraction positions below 15°. The deviation of the measured diffraction angle was ±0.05°. The crystal unit cell determination was achieved by construction of the reciprocal lattice. Solutions with the least error between calculated values and experimental results were calculated and compared with computer refinements.[53,54]

SAXS experiments were performed at beamline 23A1 at the National Synchrotron Radiation Research Center (NSRRC) located at Hsinchu, Taiwan.[55] The source energy and sample-to-detector distance were 10 keV and 2444 mm, respectively. An exposure time of about 20 seconds was required to ensure high quality patterns. The SAXS intensity profiles were plotted against $q = 4\pi\sin\theta/\lambda$, where λ is the wavelength of X-ray ($\lambda = 0.124$ nm) and 2θ is the scattering angle. The SAXS spectra were recorded by a 2D Mar CCD detector with 512 × 512 pixel resolution. Silver behenate with primary reflection peak at 1.067 nm^{-1} was used to calibrate the q value.

TEM bright field images were obtained with a JEOL (1200 EX II) TEM using an accelerating voltage of 120 kV. SAED experiments were carried out by a TEM rotating–tilting stage to provide the ED diffraction patterns and the unit cell parameters. The camera length was set in a range between 0.8 m and 1.2 m. The d-spacings were calibrated by using evaporated thallous chloride standard, which has the largest first-order spacing diffraction of 0.384 nm.

Morphological optical textures of ordered phases at the micrometre scale were observed by a polarized optical microscope (Olympus BH-2) coupled with a Mettler hot stage (FP-90). Polarizer, analyzer, and tint plate were inserted in the light path to study the molecular orientation within the supramolecular structures (results are reported in ESI†).

Molecular packing modeling and crystallographic simulation was performed using the Accelrys Cerius^2 simulation package (version 4.6) with COMPASS force field. The global equilibrium conformation with lowest energy at 0 K was chosen as the initial molecular conformation. Unit cell parameters determined *via* 1D WAXD, 2D WAXD, SAXS, and SAED patterns were adopted as initial values for constructing the simulated crystal unit cell.

Results and discussion

Synthesis of $C_{22}PhBAEO_3$

Compound $C_{22}PhBAEO_3$ (**1**) was obtained by first reacting 3,4,5-tris-docosoxybenzoic acid with excess 1,4-phenylenediamine using Steglich esterification to give a single substituted primary amine derivative ($C_{22}NH_2$, **2**). The amine derivative further underwent esterification reaction with 3,4,5-tris(2-(2-(2-hydroxyethoxy)ethoxy)-ethoxy)benzoic acid to give the desired product. The molecular purity and integrity were confirmed by ^1H NMR, ^{13}C NMR, MALDI-TOF mass spectrometry, and IR spectroscopy (see Fig. S2–S4 in ESI†). The compound possessed a light yellow color with good thermal stability. It revealed 1% weight loss at 277 °C during thermogravimetric measurement under N_2 atmosphere (Fig. S5 in ESI†).

At the bottom of Scheme 1, the geometric shape and dimension, which were constructed by Cerius^2 4.6 software, of each part of the asymmetric tapered $C_{22}PhBAEO_3$ are shown in the extended conformation. The molecule contains three parts: a core with three phenylenes connected by two amide bonds which can form hydrogen bonding with neighboring molecules during the phase formation, three hydrophobic alkyl chain tails each having 22 carbon atoms located on one side of the molecule, and three hydrophilic methyl terminated triethylene glycol tails (EO chain with three repeat units) located on the other. The hydrophobic and hydrophilic tails on both sides of $C_{22}PhBAEO_3$ are immiscible yet covalently connected with the core, therefore only micro-phase separation at a nano-scale is allowed during supramolecular structure formation. One should note that not only does the Janus asymmetric character manifest in the polarity of these two tails but also the geometrical length of the hydrophobic part is about twice that of the hydrophilic part.

Phase behavior and the corresponding structure evolution

Fig. 1a shows a set of DSC thermal diagrams of $C_{22}PhBAEO_3$ during heating and cooling. The top two scans are the cooling scan from the I melt to 40 °C and the subsequent heating of $C_{22}PhBAEO_3$. During the cooling, two thermal transition processes are found at the onset temperatures of 85 °C (with a heat of transition of −19.2 kJ mol^{-1}) and 71 °C (−83.3 kJ mol^{-1}). Upon the subsequent heating, two endothermic thermal

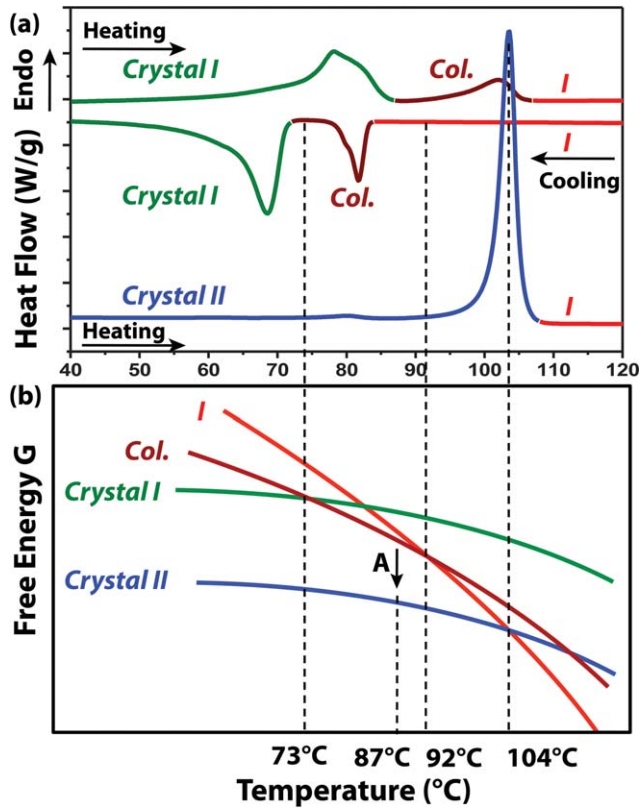

Fig. 1 DSC thermal diagrams and a Gibbs free energy–temperature (*G*–*T*) diagram of $C_{22}PhBAEO_3$ at a scan rate of 10 °C min^{-1}. (a) The top two thermal scans: a cooling diagram from the *I* phase and subsequent heating. The bottom thermal diagram: a heating diagram after annealing at 87 °C for 2 hours. (b) Schematic illustration of the free energies with respect to temperature at atmospheric pressure of the isotropic and three ordered phases (the assignments of *col*., *crystal I* and *crystal II* phases are by the structural analysis based on WAXD and ED experiments).

transitions can also be observed at a scan rate of 10 °C min^{-1} at onset temperatures of 73 °C (79.9 kJ mol^{-1}) and 92 °C (20.5 kJ mol^{-1}). Based on the heats of transitions obtained during both cooling and heating, it can be recognized that two endothermic transitions observed during heating correspond to the exothermic transitions observed in the cooling, and the high-temperature transition exhibits a slight supercooling.

If $C_{22}PhBAEO_3$ is annealed at a temperature of 87 °C for 2 hours, which is in between the two endothermic transitions observed during heating, the subsequent heating reveals the existence of another phase with an endothermic transition occurring at 104 °C with a heat of transition of 120.8 kJ mol^{-1}, as shown in the thermal diagram at the bottom of Fig. 1a. Therefore, there are three ordered phases that exist in this compound, and the compound apparently exhibits a monotropic phase behavior.[56–59]

Denoting these three phases as the high-temperature (the liquid crystal (LC) columnar phase, *col*.), low-temperature (the *crystal I*) phase as observed during cooling and heating at 10 °C min^{-1} and the annealed (the *crystal II*) phase found during the isothermal experiment, these phase structural identifications were determined *via* results of WAXD and ED experiments (see below). The phase behavior observed in DSC experiments can be explained by the Gibbs free energy–temperature (*G*–*T*) diagram of the phases as shown in this figure (Fig. 1b). The diagram reveals the relative stability of each phase (the free energy) as a function of temperature. At temperatures higher than 104 °C, the *I* phase is the most stable phase since it possesses the lowest free energy. The compound should thermodynamically transfer into the most stable *crystal II* phase when the temperature decreases and passes the cross-point between the *I* and the *crystal II* phases. However, the energy barrier in forming this *crystal II* phase is kinetically too high, and this transition is thus practically forbidden at temperatures above the *col.* phase formation at a cooling rate of 10 °C min^{-1}. The compound has to be directly transferred to the *col*. phase at 85 °C since the energy formation barrier of this LC phase is low. When the temperature passes through 73 °C, the compound enters the *crystal I* phase since it becomes more stable than the *col.* phase below the cross-point between those two phases in the *G*–*T* diagram. Annealing within the *crystal I* phase was not able to bring the compound into the *crystal II* phase. Upon heating at a rate of 10 °C min^{-1}, the *crystal I* and *col*. phases melt at 73 °C and 92 °C, respectively. However, if the compound was annealed within the *col*. phase at around 87 °C, the most stable *crystal II* phase forms. Furthermore, after the compound was quenched from the *I* phase directly to 87 °C without the formation of the *col*. phase, the *crystal II* phase did not form even within a prolonged annealing time. In other words, the *col*. phase has to be the precursor in forming the stable *crystal II* phase.

DSC experiments in Fig. 1a have provided the heat transfer information during the phase transitions. To gain insights about the phase structures and their evolution associated with the thermal transition processes, a series of 1D WAXD patterns have been acquired as shown in Fig. 2. Fig. 2a shows a set of WAXD patterns obtained during cooling starting at 110 °C. Fig. 2c shows the subsequent heating patterns. In Fig. 2a, the *I* phase is confirmed at 110 °C by the observation of two amorphous halos located at 2θ of ~6.5° and 19.5°, respectively. The high-angle halo represents the short-range order of the average distance among the amorphous chains; while, the low-angle halo may indicate the average periodicity of electron density fluctuations between the micro-phase-separated aromatic core and tails and the two types of tails. In the WAXD pattern recorded at 80 °C, the high-angle halo remained and a small peak with *d*-spacing of 0.49 nm (2θ = 18.1°) appeared that corresponds to the repeat distance between H-bonded cores. This confirms the formation of the LC columnar structure. Also, two diffraction peaks appeared in the low-angle region with *d*-spacings of 3.22 nm and 2.19 nm, respectively. The *q*-value ratio of 2 : 3 was identified, indicating that a layered structure has formed (see also the SAXS result in Fig. 4). The formation of H-bonded core columns induces the phase separation of the amphiphilic tails. The phase separation of hydrophilic and hydrophobic tails forces the columns to have parallel alignment in a smectic-like fashion within the tail interface. The layer normal direction is perpendicular to the column direction (see also Fig. 7 and 9 for simulated molecular packing results). Therefore, the lamellar diffractions are attributed to the periodic arrangement of the core columns. When the temperature decreases to 30 °C, as shown in the bottom 1D WAXD pattern of Fig. 2a (the *crystal I* phase, the magnified pattern is shown in Fig. 2b, and see also, 2D WAXD in Fig. 3b and c), two new reflection peaks

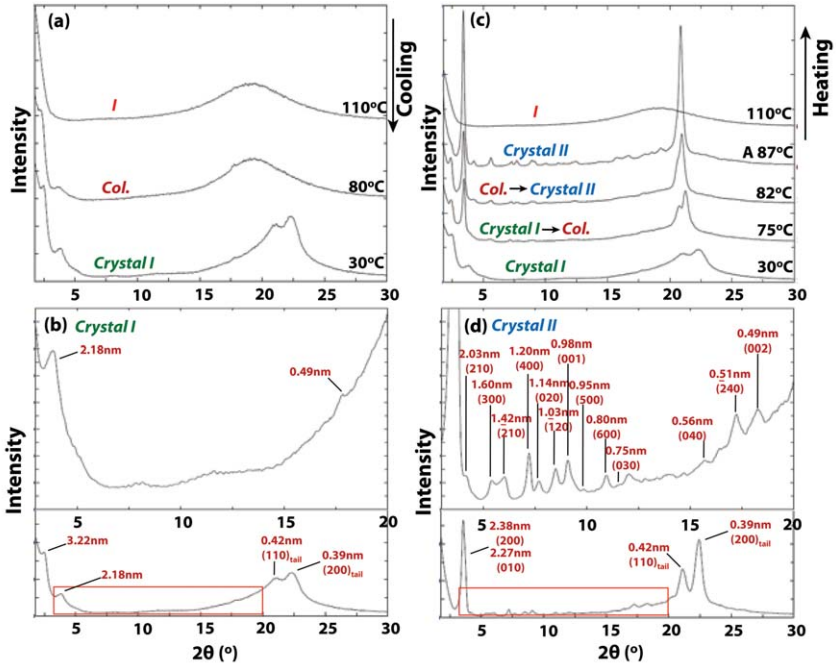

Fig. 2 Set of 1D WAXD patterns of $C_{22}PhBAEO_3$. (a) The cooling process from 110 °C to RT. (b) The enlarged *crystal I* phase pattern obtained by cooling from the *I* phase to 30 °C at cooling rate 10 °C min^{-1}. (c) The subsequent heating process from RT to 110 °C. (d) The enlarged *crystal II* phase pattern obtained by annealing the *crystal I* phase at 87 °C for 2 hours. The top patterns in (b) and (d) are the magnified results within the area marked by red rectangular boxes. A scan rate of 1° min^{-1} was used.

develop in the high-angle halo with a *d*-spacing of 0.42 nm and 0.39 nm, respectively. These two high 2θ-angle diffractions corresponded to the (110) and (200) inter-chain packing distance of the alkyl tails, respectively, which is similar to that found in ordinary polyolefin crystals.[60] The diffractions in the small angle region remain unchanged as well as the diffraction of *d*-spacing 0.49 nm corresponding to the repeat distance along the H-bonding direction (or the half-disc thickness). This indicates that the layer structure and dimension do not change during the low-temperature transition even when the alkyl tails crystallized in the hydrophobic layers with relatively random orientation and low crystallinity (simulated molecular packing results can be found in

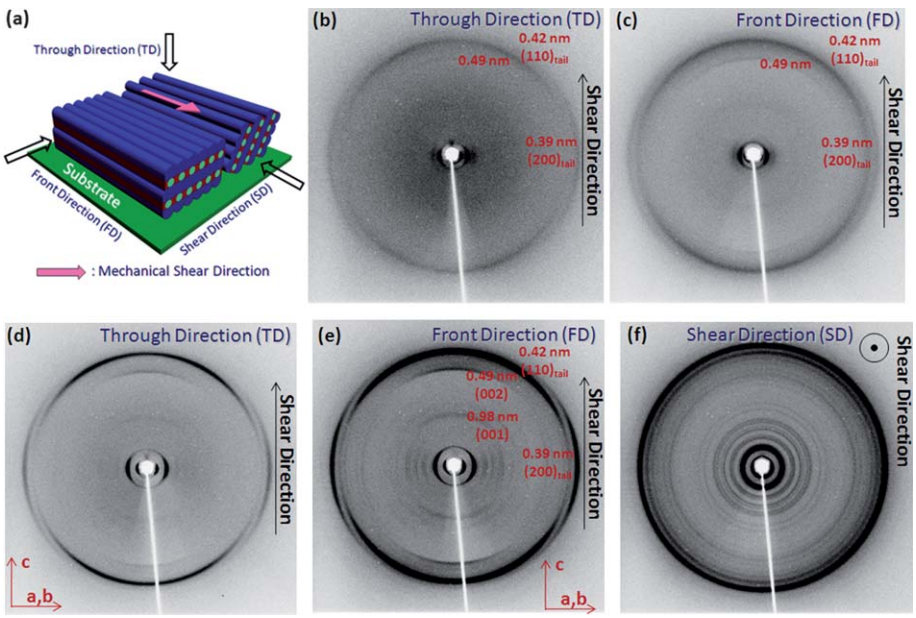

Fig. 3 2D WAXD patterns of the *crystal I* (b and c) and the *crystal II* (d, e and f) phases after shearing with incident X-ray beam along (b) and (d) the through direction (TD), (c and e) the front direction (FD), and (f) the shear direction (SD). (a) Relative orientation of sample and X-ray beam. Solid arrow indicates the direction of mechanical shearing force applied on the sample. The hollow arrows indicate the direction of the incident X-ray beam.

Fig. 9). Note that very few diffractions can be identified between $2\theta = 5°$ and 20° (Fig. 2b), indicating that the core supramolecular columns in the *crystal I* phase possess a rather poor 3D ordered packing.

Fig. 2c shows a set of 1D WAXD patterns recorded in a subsequent heating. At 82 °C, the alkyl tail crystals melt and the system undergoes a transition from a crystal structure to a "rotator phase". Note that this melting temperature is much higher than that of pure $C_{22}H_{46}$ (42 °C). This observation is similar to that made with the symmetric tapered bisamides reported before.[44–46] In $C_{22}PhBAEO_3$, the peaks of the (200) and (110) diffractions gradually merged together and completely overlapped at 82 °C, revealing a transition from the crystal to a pseudo-hexagonal rotator phase. This rotator phase has been described such that the alkyl tails rotate along the chain axis locally in the unit cell, in which the all *trans*-conformation is still kept yet the bond orientation order is lost.[61–63] This rotator phase generally appears in chains where the number of carbons is between 11 and 40 in *n*-alkenes.[61–63] It is observed that in Fig. 2c, the tails' re-organization process towards the rotator phase takes place immediately after the melting of the alkyl tail crystals (a reconstruction exothermic peak was observed immediately after the melting peak of the *crystal I* phase, as shown in Fig. S6 of ESI†). During the process of temperature equilibrium and angular X-ray scanning (1° min^{-1}), the more stable *crystal II* phase starts to develop as evidenced by the observation of the growing crystalline diffractions in the vicinity of $2\theta \sim 22°$ that start out the top of the amorphous halo in the patterns obtained above 75 °C. In the WAXD pattern collected at 87 °C, one strong low-angle diffraction peak appears at *d*-spacing of 2.38 nm ($2\theta = 3.71°$) and a set of weaker diffractions corresponding to the ordered inter-column packing spacings develops between $2\theta = 5°$and 20° (a 5× magnified WAXD pattern is included in Fig. 2d). It is evident that the packing scheme of the columns has been changed as compared with the *crystal I*, and the long-range order of this *crystal II* structure has been improved within the isothermal annealing time period of the WAXD data collection at 87 °C. A strong diffraction observed at $2\theta = 20.8°$ results from the crystalline rotator phase of the alkyl tails.[61–63] It is actually a merge of the (110) and (200) diffractions of the alkyl chain that gradually form a pseudo-hexagonal packing. The thermal expansion coefficient of the (200) plane is larger than that of the (110) plane, and as the (200) spacing increases, the two diffractions gradually merge to become one during heating (the evidence can be found in a series of WAXD patterns obtained during heating in Fig. S9 of ESI†).

Fig. 2d shows the 1D WAXD pattern of the *crystal II* phase collected at room temperature. The two separated diffractions between $2\theta = 21°$ and 24° are attributed to the alkyl tail ordered packing that returns to crystals from the rotator phase during cooling. The (*hkl*) plane index assignments of the stable *crystal II* phase in Fig. 2d are obtained based on the structure determination *via* combined 2D WAXD, SAXS, and SAED experiments (see below). Furthermore, this *crystal II* phase cannot be achieved by directly quenching the sample from the *I* phase to 87 °C even if annealed there for one day as shown in supporting DSC and XRD results located at Fig. S7 and S8 in ESI†, respectively. The result again indicated that the *col.* phase has to be the precursor of *crystal II* phase.

Supramolecular structure determinations of $C_{22}PhBAEO_3$

A combination of the DSC and 1D WAXD results provides the structure evolution of $C_{22}PhBAEO_3$. Experimental techniques of SAXS and 2D WAXD can provide more insight about the detailed supramolecular structures and packing symmetry. Fig. 3 shows the 2D WAXD patterns of the *crystal I* and *crystal II* phases after mechanical shearing. For the *crystal I* phase, the sample was sheared within the *col.* phase (at 75 °C). The geometric orientation of the incident X-ray beam with respect to the sheared sample is shown in Fig. 3a. Fig. 3b and c are 2D patterns of the *crystal I* phase obtained from the through and front directions (TD and FD), respectively. These two patterns are essentially identical. In the low-angle region along the equator (<5°), two arcs of *d*-spacing at 3.22 nm ($2\theta = 2.74°$) and 2.18 nm ($2\theta = 4.04°$), with a *q*-value ratio of 2 : 3, can be observed, revealing again a layered structure parallel to the column axis that shows a periodic change of the electron density along the lateral direction of the aligned column axis. In the high-angle region (>5°) along the meridian direction, an arc with *d*-spacing 0.49 nm appeared that corresponds to the bisamide core-to-core distance along the hydrogen bonding direction.[44–46] The (200) arc at $2\theta = 21.2°$ along the equator and the (110) arc at $2\theta = 22.8°$ in the quadrant are attributed to the packing of the tail crystals and their orientation.[60] This is thus a "fiber pattern" of the alkyl chain crystals with the *b*-axis along the fiber (column) direction. In other words, the *b*-axis of the tail crystals is parallel to the shear direction and thus, the column axis. Comparison between experimental and simulated X-ray fiber patterns of alkyl chain crystals is located in Fig. S10 in ESI†.

Fig. 3d–f are 2D WAXD patterns of the *crystal II* phase obtained along the TD, FD, and SD, respectively, for the sample obtained by heating the *crystal I* phase to 87 °C and annealed there for 2 hours. Two patterns shown in Fig. 3d and e are identical with an arc of a *d*-spacing of 0.49 nm along the meridian direction. This again suggests that the columnar structure remained unchanged along the column axis within the *crystal II* phase and that this column axis is parallel to the shear direction. However, the lateral packing of the columns becomes different. Compared with the 2D WAXD patterns of *crystal I*, the two strong arcs appearing in the small 2θ angle region now are at *d*-spacings of 4.79 nm ($2\theta = 1.84°$) and 2.38 nm ($2\theta = 3.71°$), respectively. In addition, many relatively weak diffraction arcs can be observed between $2\theta = 5°$ and 20° on the equator and quadrants, revealing a better 3D packing of the bisamide core columns in the *crystal II* phase. The arcs corresponding to the alkyl tail crystals remained at the same positions as in the case of *crystal I* since this 2D WAXD pattern was taken at room temperature. These diffractions are stronger and sharper due to a higher crystallinity and better ordered crystals. The tails preserved the original orientation after the tail rearrangement in *crystal II*. It is evident that the layer arrangement of smectic-like columnar structure of the bisamide cores in the *crystal I* and *col.* phases has changed into a long-range ordered supramolecular crystalline structure according to the spacing shift in the small-angle region and the appearance of the inter-column order diffractions on the equator. Moreover, the layer structure from the phase separation of tails must remain in the *crystal II* phase.

The ring pattern obtained along the shear direction in Fig. 3f provides additional evidence to prove that Fig. 3d and 3e are fiber patterns of the *crystal II* phase. The tail packing orientation is again aligned along the *b*-axis of the alkyl chain unit cell and the SD at room temperature. In the core packing, the column axis (the *c*-axis) is parallel to the SD (along the meridian), while the *a*- and *b*-axes are rotating within the equator plane. Based on these patterns, the α and β angles of the unit cell can thus be determined to be 90.0°, and the dimension of *c*-axis can be measured as 0.98 nm. According to the information collected thus far, the crystal structure lattice of the supramolecular core packing in the *crystal II* phase could be either orthorhombic or monoclinic.

SAXS experiments were conducted to confirm the actual phase structures, and the results are shown in Fig. 4. In this figure, the bottom pattern is obtained from the *crystal I* phase. The layered structure is confirmed due to the observation of diffraction peaks with *d*-spacings of 6.41, 3.22, and 2.18 nm which possess *q* value ratios of 1 : 2 : 3. This layer structure, with the layer normal perpendicular to the columnar direction, is formed due to both the phase separation of the hydrophilic and hydrophobic tails and the formation of core columns at the interface of the two kinds of tails. The phase separation behaviour of the tails gives rise to the individual supramolecular column to exhibit a Janus character. Furthermore, it also explains why the *col.* phase plays an important role as a precursor in the formation of the stable *crystal II* phase since the molecular lateral packing and the crystallinity evolution have to be based on the phase-separated layers which form after the formation of supramolecular columns.

The top pattern in Fig. 4 is the SAXS data obtained from the *crystal II* phase at room temperature. Four diffraction peaks with $2\theta = 1.84°$, 3.71°, 3.89°, and 4.38°can be identified from the pattern. As discussed above, the diffractions in this pattern are dominated by the packing of the cores. Based on the triangulation 2D lattice building method,[53,54] the four diffractions were assigned as the (100), (200)/(110), (010), and (210) diffractions, respectively. Note that the second diffraction is an overlap of the (200) and (110) diffractions with *d*-spacings of 2.39 nm and 2.38 nm. The high resolution SAXS results reveal that the strong peak observed at $2\theta = 3.71°$ in both 1D and 2D WAXD is actually an overlap of the (200)/(110) diffractions with *d*-spacings of 2.39 nm and 2.38 nm. With this piece of information in hand and combined with all other diffractions observed in the WAXD patterns, a 2D a^*b^* lattice can be constructed to fit with all the diffractions on the equator of the 2D WAXD pattern. Careful structural analysis *via* the refinement of the reciprocal lattice reveals a monoclinic unit cell with dimensions of $a = 5.08$ nm, $b = 2.41$ nm, $c = 0.98$ nm, $\alpha = \beta = 90.0°$, and $\gamma = 70.5°$, which fits the best to the experimental diffraction results.

Crystallographic density calculations based on the molecular weight of $C_{22}PhBAEO_3$ (1776.66 g mol^{-1}) and the unit cell volume (11.31 nm^3) give rise to a theoretical density of 1.04 g cm^{-3} with four molecules per unit cell. The theoretical value matches well with the experimentally measured one, 1.03 g cm^{-3}. Fig. 5a shows the 2D WAXD pattern of the *crystal II* phase with the mechanical shearing direction marked as SD. The diffractions on the meridian are indexed according to the monoclinic unit cell determined above as shown in Fig. 5b (see also in Fig. 2d). Those on the equator are also indexed as shown in Fig. 5c. Table 1 is the list of experimentally observed and calculated *d*-spacings and 2θ values according to the unit cell parameters.

A bright field TEM image of the *crystal I* phase is shown in Fig. 6a. Concentric circular bands were observed parallel to the tangential circular boundary. The PE-SLD result shown in Fig. 6b shows the existence of columns that are constructed by the H-bonded aromatic cores wrapped with the amphiphilic flexible tail shell. The PE fragments are deposited between the

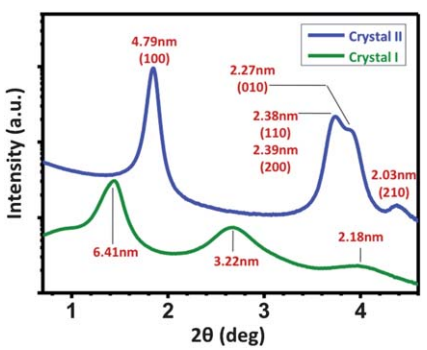

Fig. 4 SAXS patterns of the *crystal I* and *crystal II* phases. Top pattern: the *crystal II* phase obtained by annealing the *crystal I* phase at 87 °C for 2 hours. Bottom pattern: the *crystal I* phase obtained by cooling from the *I* phase to RT at a cooling rate of 10 °C min^{-1}.

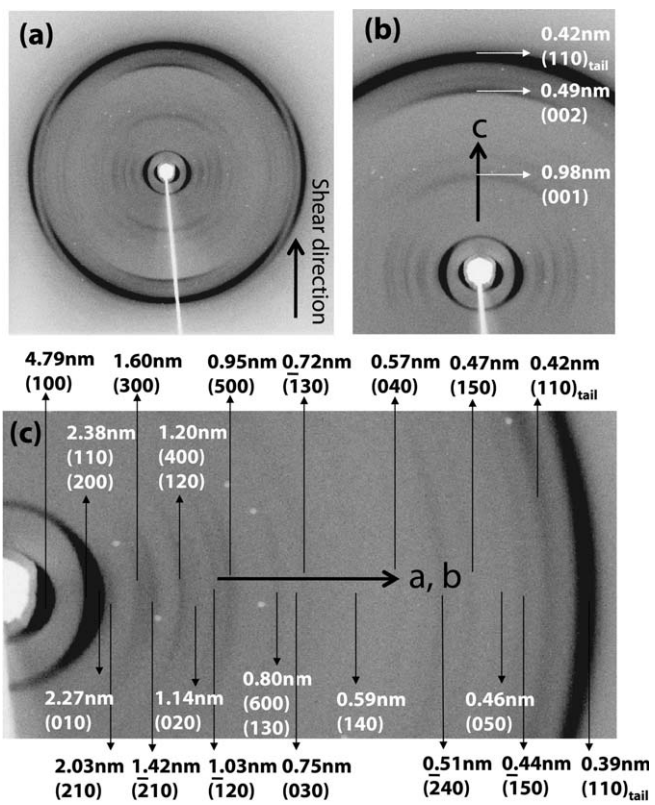

Fig. 5 2D WAXD pattern of the mechanically sheared *crystal II* phase (a). The assignment of meridian diffractions (b) and equatorial diffractions (c) between $2\theta = 4.7°$ and 21.5° based on the 2D a^*b^* lattice.

Table 1 Crystallographic parameters of C_{22} PhBAEO_3 bisamide *crystal II* phase monoclinic crystals

		2θ/°		*d*-spacing/nm	
No.	(*hkl*)	Exptl[a]	Calc.[b]	Exptl[a]	Calc.[b]
1	(100)	1.84	1.84	4.79	4.79
2	(110)(200)	3.71	3.71, +3.69	2.38	2.38, +2.39
3	(010)	3.89	3.89	2.27	2.27
4	(210)	4.36	4.38	2.03	2.02
5	(300)	5.52	5.54	1.60	1.60
6	(210)	6.23	6.19	1.42	1.43
7	(400)(120)	7.35	7.38, +7.38	1.20	1.20, +1.20
8	(020)	7.74	7.79	1.14	1.13
9	(120)	8.58	8.58	1.03	1.03
10	(001)	9.02	9.02	0.98	0.98
11	(500)	9.27	9.23	0.95	0.96
12	(600)(130)	11.09	11.08, +11.21	0.80	0.80, +0.79
13	(030)	11.74	11.69	0.75	0.76
14	(130)	12.33	12.43	0.72	0.71
15	(140)	15.05	15.09	0.59	0.59
16	(040)	15.69	15.61	0.56	0.57
17	(240)	17.26	17.21	0.51	0.51
18	(002)	18.10	18.10	0.49	0.49
19	(112)	18.42	18.49	0.48	0.48
20	(150)	18.89	19.00	0.47	0.47
21	(050)	19.53	19.55	0.45	0.45
22	(222)	19.62	19.59	0.45	0.45
23	(150)	20.35	20.25	0.43	0.44
24	(332)	21.22	21.31	0.42	0.42
25	(060)	23.65	23.51	0.38	0.38

[a] Experimental values observed in both WAXD and TEM. [b] Calculated based on the monoclinic unit cell of $a = 5.08$ nm, $b = 2.41$ nm, $c = 0.98$ nm, and $\alpha = \beta = 90°$, $\gamma = 70.5°$.

edges of two columns and then, crystallized to form rod-like edge-on crystals.[49,50] In other words, the PE chains are parallel to the column axis, and the long axis of the PE rod-like crystals is perpendicular to it (the *c*-axis of the PE crystals is parallel to the column direction). According to the PE crystal orientation in the image, the column axis is judged to be perpendicular to the radius direction of the circular bands (parallel to the tangential direction of the circular bands). Fig. 6c shows an image of the *crystal II* phase obtained after annealing the same grid at 87 °C for 2 hours. The images show a straight lath-like morphology. The texture difference between the two phases can be readily identified, indicating the characteristics of different structures between these two phases. Single crystal SAED patterns were obtained from a single *crystal II* domain (for example, the circled area in Fig. 6c), and the relative orientation between columns and alkyl tails was deduced based on the ED pattern (see discussion below). Fig. 6d shows the PE-SLD result of the *crystal II* phase. The ordered PE rods reveal that the column orientation in the *crystal II* phase is along the long axis of the lath-like crystal. The difference of this decoration pattern compared with that of the *crystal I* is clearly seen, indicating different supramolecular column arrangement near the crystal surface. Mixed *crystal I* and *crystal II* phases during the transition can also be observed as shown in Fig. 6e. The *crystal II* single crystals are extruded out from the circular *crystal I* morphology. Fig. 6f is the PE-SLD pattern on the mixture of the two phases. The regions of the *crystal I* and *crystal II* can be distinguished by the difference in decoration patterns as well as the phase textures. We speculate that the morphological difference is attributed to the crystallinity difference of the alkyl tails in these two phases. In the *crystal I* phase, the alkyl chain tails possess low crystallinity and less molecular orientation and thus, have a lower modulus. This may lead to the bent, circular morphology. On other hand, the alkyl tails in *crystal II* phase possess higher positional and molecular orientational order even when they are in the rotator phase (see XRD and ED results in Fig. 2, 3 and 8). A higher modulus and the straight lath-like morphology are thus observed in the *crystal II* phase. The alkyl tails in the *crystal II* phase crystallized toward extended chain and interdigitated conformations (simulation results locate in Fig. 8 and 9); therefore, the boundaries between columns, which will direct the PE rods orientation, become blurred and lead to a different and less orientationally ordered PE-SLD pattern compared with *crystal I* (Fig. 6).

Molecular packing of the stable *crystal II* phase

According to the experimental results obtained, we were able to construct a packing model of the *crystal II* phase through

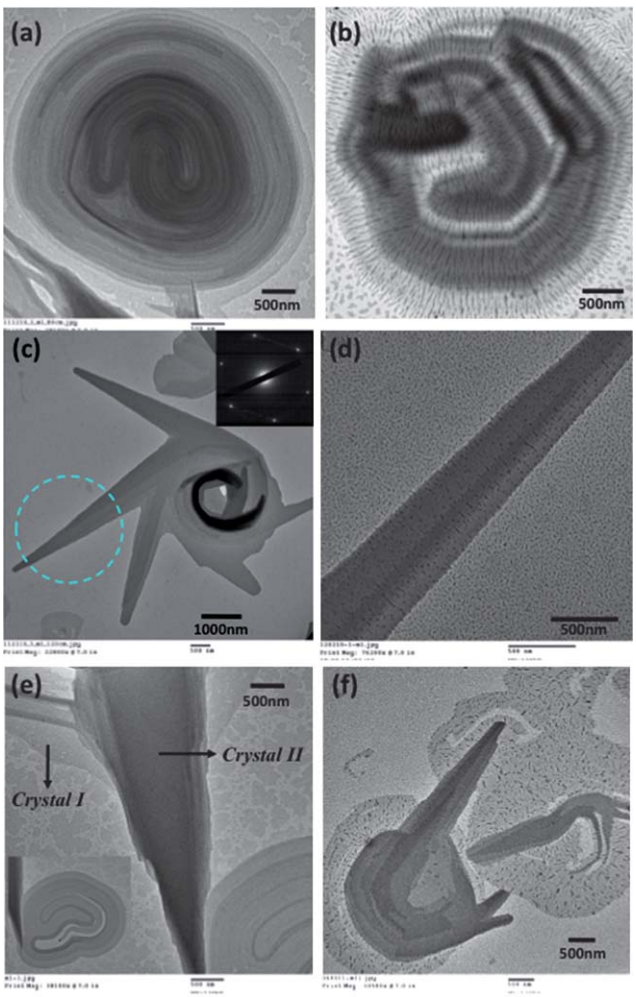

Fig. 6 TEM bright field images of (a) the *crystal I* phase, (b) the *crystal I* phase after PE-SLD, (c) the *crystal II* phase obtained after annealing at 87 °C, (d) PE-SLD on *crystal II* phase, (e) mixture of the *crystal I* and *crystal II* phases during phase transition, (f) PE-SLD on a mixture of two phases.

molecular packing simulation and energy minimization. This model involves hierarchical structures at different length scales. The first level of the structure is a 2D phase separated disc constructed as shown in Fig. 7a (top view). Fig. 7b is a side view. In these two figures, the hydrophobic tails are in blue and hydrophilic tails are in red for clarity. It can be seen that the disc is separated into four sectors. The alkyl tails and TEG tails both occupy two sectors in diagonal locations. The step-by-step disc formation mechanism is proposed in Fig. S11 in the ESI†. This arrangement will mediate the unbalanced stress within the disc between the two tails of different sizes. Each disc contains four $C_{22}PhBAEO_3$ Janus molecules, separated into two pairs. According to the global energy minimization result, two aromatic cores in the top pair adopt a face-to-face conformation at a distance of 0.7–1.0 nm apart from each other. The other pair of two cores located at the bottom adopts the same conformation but rotates by 90°. The center-to-center distance between the two pairs (the half-height of one disc) is about 0.49 nm as observed in WAXD experiments, and they are connected by four hydrogen bonds located at the aromatic core cross-points shown in Fig. 7a. This structure can be stabilized due to the fact that the amide cores are self-assembled through intermolecular hydrogen bonding between neighboring C═O and N–H groups with a distance of 0.28 nm.[46,47] A molecular disc packing model containing both cores and tails is constructed by Cerius^2 4.6 software using the COMPASS force field. The schematic illustration is shown in Fig. 7c. Due to the size difference of the tails, the disc possesses an ellipsoid shape with the hydrogen bonded amide core represented as a solid green circle.

The second level of the structure is the asymmetric ellipsoid cylinder, attributed to stacking of the discs. Instead of π–π stacking between discs in traditional columnar LCs, all discs are connected by the intermolecular hydrogen bonding to build up the bisamide supramolecular structure. Illustrations of the 1D ellipsoid columns and the perspective view of the supramolecular structure of the *crystal II* phase can be found in Fig. 7c. The amphiphilic ellipsoid discs stack together to form phase-separated columns with the hydrogen bonding direction parallel to the column axis.

The third level of structure in the *crystal II* structure is constructed *via* the packing of these columns. Flexible hydrophilic tails that remain amorphous in the *crystal II* phase are represented as a red rectangle located at the top and bottom sides of the core. Crystalline hydrophobic tails which possess a zigzag extended chain conformation in the *crystal II* phase at room temperature are represented as a blue semi-ellipsoid located on the other two sides of the core. A monoclinic unit cell with

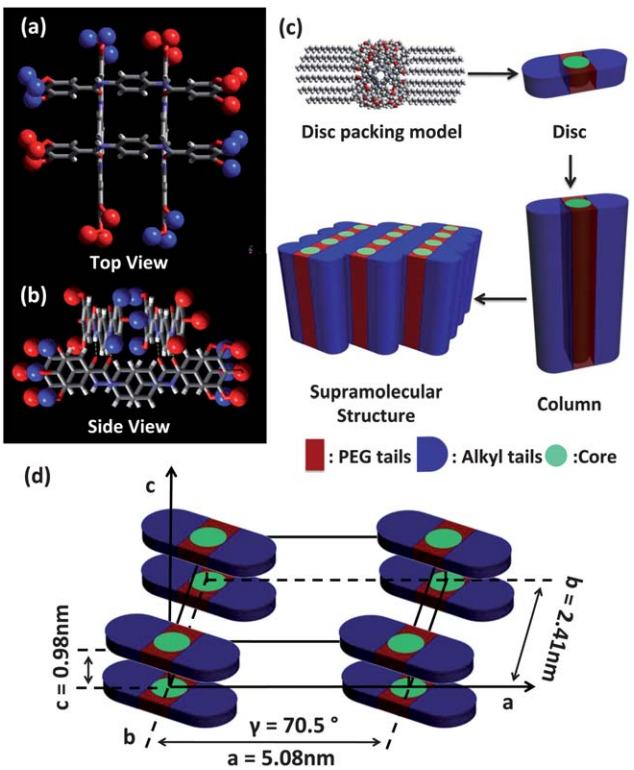

Fig. 7 Top (a) and side (b) views of the Janus disc packing model. Hydrophilic tails are represented as red balls, and hydrophobic tails are represented as blue balls. (c) Computer constructed molecular packing model inside a disc and illustrations of structure migration from 2D asymmetric disc to 3D supramolecular structure. (d) Schematic unit cell model with four molecules (one disc) for the 3D *crystal II* phase of $C_{22}PhBAEO_3$.

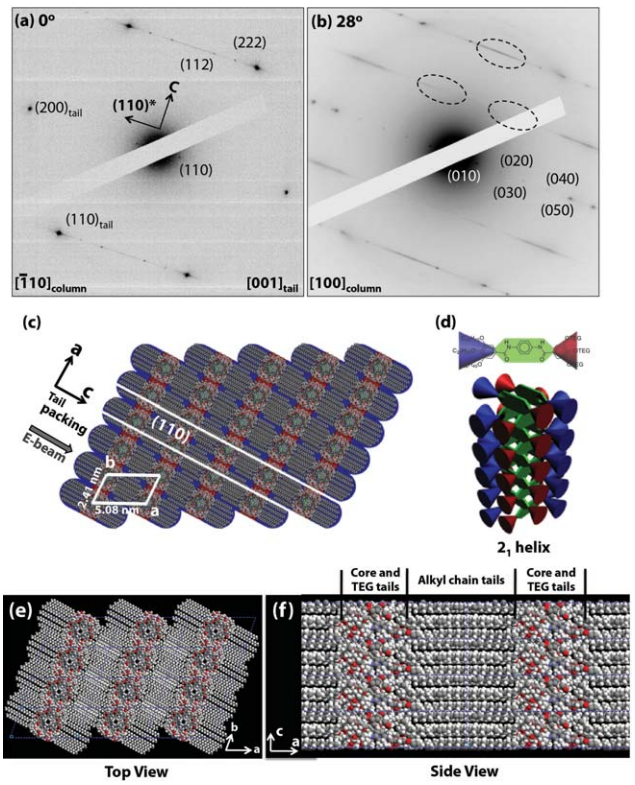

Fig. 8 (a) SAED pattern of the circled area of the bright-field TEM image in Fig. 6c. (b) SAED pattern obtained after clockwise tilting 28° along the *c*-axis of the pattern in (a). (c) Schematic illustration of the molecular arrangement of the supramolecular structure packing in the monoclinic unit cell. Relative orientation between columns and tails in the hierarchical structure is illustrated. (d) Schematic representation of the 2_1 helix packing of the molecular pairs. Computer simulated molecular packing of $C_{22}PhBAEO_3$ in the crystal lattice on (e) *ab*-plane when projected from the *c*-axis and (f) *ac*-plane when projected from the *b**-axis.

alternating hydrophobic and hydrophilic layers can thus be constructed, and the layer normal is perpendicular to the *b*-axis. The alkyl chain tails are partially "confined" and crystallized within the hydrophobic layers and therefore, a hierarchical structure is generated. The phase separation of hydrophilic–hydrophobic tails is induced during the formation of H-bonded aromatic columns. The supramolecular core columns are thus embedded within the amphiphilic tail interface during the formation of third level hierarchical structure.

Through the crystal structure analysis above, the cell parameters of $a = 5.08$ nm, $b = 2.41$ nm, $c = 0.98$ nm, $\alpha = \beta = 90.0°$, and $\gamma = 70.5°$ were determined. A schematic of molecular packing in the unit cell of the supramolecular structure was built and shown in Fig. 7d. Four molecules are accommodated in one unit cell based on the density measurement. In addition, each ellipsoid disc also contains four molecules stabilized by H-bonding as shown in Fig. 7a. Therefore, the crystal must possess a primitive lattice that has eight discs at the eight corners. This leads to one disc per unit cell. Based on the cell parameters determined, the crystal system is primitive monoclinic with space group assigned as *P*2/*m* (no. 10). The *c*-axis is the H-bonding direction and the stacking of discs along *c*-axis produced the supramolecular columns.

The relative orientation between the packing of alkyl tails and the aromatic core columns was derived from the SAED experiments on a single domain of the *crystal II* phase as shown in Fig. 8a. The pattern was obtained from the circled area of the bright field image in Fig. 6c. Two sets of overlapped SAED patterns can be identified. The weaker diffractions are attributed to the packing of aromatic columns and the six strong diffractions are attributed to the tail packing. In the column packing, a pair of spots with the smallest *q* value closest to the main beam has a *d*-spacing of 2.38 nm and agrees with the (110) diffraction at $2\theta = 3.7°$ on the equator of the SAXS and 2D WAXD results. Another two pairs of weaker diffractions with *d*-spacings of 0.48 nm and 0.45 nm belong to the (112) and (222) diffractions, respectively. This indicates that the *c*-axis direction is parallel to the substrate as shown on the pattern, and the zone for this pattern is determined to be $[\bar{1}10]$ for the column packing. Six bright spots in the pattern belong to the diffractions of the alkyl tail packing. They can be assigned as the (110) and (200) diffractions as labeled which indicates that this is the [001] pattern of the tail packing.

According to the analysis, the *a*-axis of the crystals formed by the alkyl tails is perpendicular to the (110) plane of the column packing, while its *b*- and *c*-axes are parallel to it. Consistent with the 2D-WAXD results (Fig. 3d and e), the *b*-axis of the alkyl crystals is also parallel to the *c*-axis of the supramolecular crystals formed by the columns. The [100] zone pattern of the supramolecular crystals can be obtained by rotating the crystal along its *c*-axis. Fig. 8b shows a pattern obtained by 28° clockwise rotation along the column *c*-axis. The diffraction spots belonging to the (010), (020), (030), (040), (050), and (060) on the *b**-axis of the supramolecular crystal were identified. This confirms the unit cell determination and *d*-spacing calculations as discussed in the above sections. The streaks appearing in the diffraction patterns in Fig. 8b (circled by dashed ellipsoids) may come from packing imperfections introduced by the unbalanced stress.[64,65] Another possibility may be reminiscent of a helical pattern found in a 2_1 helix.[66] This feature could result from the alternate rotation character of the molecular pairs as shown in Fig. 7 and 8d. An illustration of the *ab*-plane combined with column packing and tail packing is shown in Fig. 8c. Note that the alkyl tails crystallized within the hydrophobic layers with the chain axis (*c*-axis) perpendicular to the column axis and parallel to the (110) plane of the supramolecular crystals according to the SAED patterns. The computer simulated model constructed by Accelrys Cerius^2 package using the COMPASS force field is shown in Fig. 8e and f. The model represents the most probable molecular packing of $C_{22}PhBAEO_3$ in the monoclinic unit cell and agrees well with the hierarchical structure determined above. The phase morphologies of the *crystal I* and *crystal II* phases observed under POM with and without the tint plate, which provided further evidence for the hierarchical structure determination discussed, can be found in Fig. S12 in the ESI†.

Based on their structural characteristics, we can summarize these three ordered phase structures as shown in Fig. 9. In the *columnar* phase (Fig. 9a), the aromatic columns have smectic-like arrangement within an amorphous yet phase-separated matrix consisting of flexible tails. The columns are periodically arranged within the tail interface to give a layer structure, but the lateral order of columns is absent. In the *crystal I* phase (Fig. 9b), the spacing of the layers remains unchanged but a portion of the alkyl tails crystallized within the hydrophobic layer (the circled area) with less ordered chain orientation. In the *crystal II* phase (Fig. 9c), the aromatic columns pack into a 3D long-range ordered monoclinic unit cell in which the alkyl tails are interdigitated and possess high crystallinity with a generally fixed chain orientation.

It is interesting that the transformation and amplification of Janus feature is similar to the concept of chirality transformation and amplification.[67–69] In this case, its Janus feature transfers and amplifies from the molecular level to the disc motif, inducing the formation of an ellipsoid disc. This transformation further takes

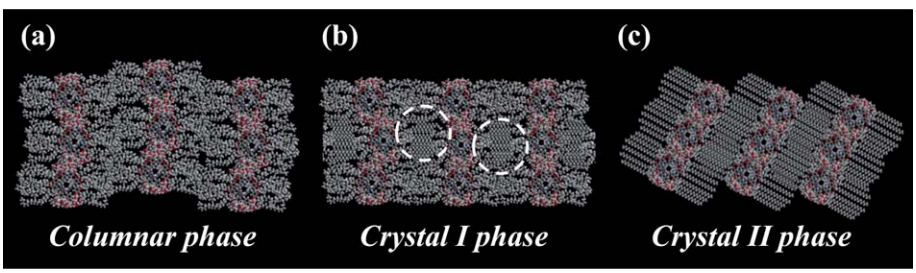

Fig. 9 Simulated molecular packing models for (a) *columnar* phase, (b) *crystal I* phase, and (c) *crystal II* phase.

place to form the asymmetric column. After multiple columns self-assemble into the supramolecular structure, although the phase-separation character remains, the transformation and amplification of this Janus feature stop as a typical principle of transformation and amplification of the Janus effect *via* hierarchal structure.[70]

Conclusions

In summary, an asymmetric-tapered Janus bisamide, $C_{22}PhBAEO_3$, has been designed and synthesized. The evolution of its hierarchical supramolecular structure through levels of different length scales and thermotropic phase behavior have been fully characterized. The molecule consists of a rigid amide core and three flexible tails with different lengths and chemical properties on either side. It has been found that the molecules formed three levels of hierarchical structures. The first level is a phase-separated disc consisting of four Janus bisamide molecules connected by H-bonding. The second level is an asymmetric supramolecular column constructed by the stacking of discs. The column has a ridged aromatic core and flexible amphiphilic shells. The third level is a 3D ordered assembly of columns while still keeping the phase-separated character of the tails within the structure. In addition, three phases with different orders for the highest hierarchical structure are identified before the temperature reaches the isotropic *I* phase. They are assigned as the *crystal II* phase, the *crystal I* phase, and the *col.* phase. These three phases possess phase-separated columnar structures. Monotropic phase behavior has been identified by thermal analysis. It has been found that the *col.* phase and *crystal I* phase form at 85 °C and 75 °C during cooling, respectively. The *crystal II* phase forms during annealing under the precursor *col.* phase and melts at 104 °C. Morphologies have been studied through bright field TEM images. The existence of a columnar structure has also been confirmed by PE-SLD technique in both crystal phases. *Crystal I* has a concentric ring morphology due to the smectic-like arrangement of aromatic columns and the low crystallinity of alkyl tails. *Crystal II* possesses a straight, lath-like morphology due to the dense packing of the columns and high crystallinity of the alkyl tails. The structure formation can be attributed to three major driving forces, including micro-phase separation between hydrophobic and hydrophilic tails, micro-phase separation between rigid amide cores and flexible tails, and hydrogen bond formation between N–H and C═O groups. Combining data from 1D WAXD, 2D WAXD, SAXS, and SAED experiments, detailed unit cell parameters and a supramolecular packing model of the stable *crystal II* phase were determined. The alkyl chain tails crystallized within the hydrophobic layers at low temperature and transitioned to the rotator phase at elevated temperatures. The relative orientation of the alkyl tail and aromatic core packing was also determined through SAED experiments. It is also noted that transformation and amplification of the Janus feature proceeded up to the level of an asymmetric column. Further assembly in an even larger length scale does not extend this transformation and amplification process.

Compared with the results reported in the symmetric-tapered counterparts, we have demonstrated that the motif's shape and the ratio of unit cell parameters have been significantly changed. A new *crystal II* phase has been discovered in this Janus molecule system which was not observed previously in symmetric tapered bisamides even when the length of alkyl tails was changed significantly. We speculate that the reason for structural difference is symmetry breaking of the supramolecular building blocks (discs and columns). Although the aromatic cores possess similar 2_1 helix arrangement, the resulting supramolecular columns of symmetric-tapered bisamides preserve a circular cylindrical shape that is considered as C_∞ symmetry. The phase separation behavior and size difference of the tails in asymmetric-tapered bisamides reduced the column's symmetry from C_∞ to C_2 along the column axis. The results provided a new pathway of fine-tuning not only the Janus supramolecular structures but also the design of forming the self-assembling process in order to meet the specific requirements for optical and biological applications.

Acknowledgements

This work was supported by NSF (DMR-0906898).

References

1 P.-G. de Gennes, *Angew. Chem., Int. Ed. Engl.*, 1992, **31**, 842–845.
2 B. P. Binks, *Curr. Opin. Colloid Interface Sci.*, 2002, **7**, 21–41.
3 B. P. Binks and P. D. I. Fletcher, *Langmuir*, 2001, **17**, 4708–4710.
4 J. N. Anker, C. Behrend and R. Kopelman, *J. Appl. Phys.*, 2003, **93**, 6698–6700.
5 J. N. Anker, C. J. Behrend, H. Huang and R. Kopelman, *J. Magn. Magn. Mater.*, 2005, **293**, 655–662.
6 C. J. Behrend, J. N. Anker and R. Kopelman, *Appl. Phys. Lett.*, 2004, **84**, 154–156.
7 C. J. Behrend, J. N. Anker, B. H. McNaughton, M. Brasuel, M. A. Philbert and R. Kopelman, *J. Phys. Chem. B*, 2004, **108**, 10408–10414.
8 C. J. Behrend, J. N. Anker, B. H. McNaughton and R. Kopelman, *J. Magn. Magn. Mater.*, 2005, **293**, 663–670.
9 J. Choi, Y. Zhao, D. Zhang, S. Chien and Y. H. Lo, *Nano Lett.*, 2003, **3**, 995–1000.
10 T. Nisisako, T. Torii, T. Takahashi and Y. Takizawa, *Adv. Mater.*, 2006, **18**, 1152–1156.
11 R. Golestanian, T. B. Liverpool and A. Ajdari, *Phys. Rev. Lett.*, 2005, **94**, 220801.
12 J. R. Howse, R. A. L. Jones, A. J. Ryan, T. Gough, R. Vafabakhsh and R. Golestanian, *Phys. Rev. Lett.*, 2007, **99**, 048102.
13 N. Glaser, D. J. Adams, A. Boeker and G. Krausch, *Langmuir*, 2006, **22**, 5227–5229.
14 Y. Nonomura, S. Komura and K. Tsujii, *Langmuir*, 2004, **20**, 11821–11823.
15 I. Bury, B. Heinrich, C. Bourgogne, D. Guillon and B. Donnio, *Chem.–Eur. J.*, 2006, **12**, 8396–8413.
16 M. Lattuada and T. A. Hatton, *Nano Today*, 2011, **6**, 286–308.
17 K. J. Lee, J. Yoon and J. Lahann, *Curr. Opin. Colloid Interface Sci.*, 2011, **16**, 195–202.
18 A. Walther and A. H. E. Muller, *Soft Matter*, 2008, **4**, 663–668.
19 F. Wurm and A. F. M. Kilbinger, *Angew. Chem., Int. Ed.*, 2009, **48**, 8412–8421.
20 T. Higuchi, A. Tajima, K. Motoyoshi, H. Yabu and M. Shimomura, *Angew. Chem., Int. Ed.*, 2008, **47**, 8044–8046.
21 Z. Li, M. A. Hillmyer and T. P. Lodge, *Macromolecules*, 2006, **39**, 765–771.
22 F. Wurm, H. M. Koenig, S. Hilf and A. F. M. Kilbinger, *J. Am. Chem. Soc.*, 2008, **130**, 5876–5877.
23 V. Percec, M. R. Imam, T. K. Bera, V. S. K. Balagurusamy, M. Peterca and P. A. Heiney, *Angew. Chem., Int. Ed.*, 2005, **44**, 4739–4745.
24 V. Percec, D. A. Wilson, P. Leowanawat, C. J. Wilson, A. D. Hughes, M. S. Kaucher, D. A. Hammer, D. H. Levine, A. J. Kim, F. S. Bates, K. P. Davis, T. P. Lodge, M. L. Klein, V. R. H. De, E. Aqad,

B. M. Rosen, A. O. Argintaru, M. J. Sienkowska, K. Rissanen, S. Nummelin and J. Ropponen, *Science*, 2010, **328**, 1009–1014.
25 K.-U. Jeong, J.-H. Jang, D.-Y. Kim, C. Nah, J. H. Lee, M.-H. Lee, H.-J. Sun, C.-L. Wang, S. Z. D. Cheng and E. L. Thomas, *J. Mater. Chem.*, 2011, **21**, 6824–6830.
26 G. Cheng, A. Boeker, M. Zhang, G. Krausch and A. H. E. Mueller, *Macromolecules*, 2001, **34**, 6883–6888.
27 M. Zhang and A. H. E. Mueller, *J. Polym. Sci., Part A: Polym. Chem.*, 2005, **43**, 3461–3481.
28 Z. Nie, W. Li, M. Seo, S. Xu and E. Kumacheva, *J. Am. Chem. Soc.*, 2006, **128**, 9408–9412.
29 L. Hong, S. Jiang and S. Granick, *Langmuir*, 2006, **22**, 9495–9499.
30 K.-H. Roh, D. C. Martin and J. Lahann, *Nat. Mater.*, 2005, **4**, 759–763.
31 T. Tanaka, R. Nakatsuru, Y. Kagari, N. Saito and M. Okubo, *Langmuir*, 2008, **24**, 12267–12271.
32 R. Erhardt, A. Boeker, H. Zettl, H. Kaya, W. Pyckhout-Hintzen, G. Krausch, V. Abetz and A. H. E. Mueller, *Macromolecules*, 2001, **34**, 1069–1075.
33 R. Erhardt, M. Zhang, A. Boeker, H. Zettl, C. Abetz, P. Frederik, G. Krausch, V. Abetz and A. H. E. Mueller, *J. Am. Chem. Soc.*, 2003, **125**, 3260–3267.
34 H. Xu, R. Erhardt, V. Abetz, A. H. E. Mueller and W. A. Goedel, *Langmuir*, 2001, **17**, 6787–6793.
35 S.-H. Kim, S.-J. Jeon, W. C. Jeong, H. S. Park and S.-M. Yang, *Adv. Mater.*, 2008, **20**, 4129–4134.
36 Y. Yin, Y. Lu, B. Gates and Y. Xia, *J. Am. Chem. Soc.*, 2001, **123**, 8718–8729.
37 Y. Yin, Y. Lu and Y. Xia, *J. Am. Chem. Soc.*, 2001, **123**, 771–772.
38 Y. Li, W.-B. Zhang, I. F. Hsieh, G. Zhang, Y. Cao, X. Li, C. Wesdemiotis, B. Lotz, H. Xiong and S. Z. D. Cheng, *J. Am. Chem. Soc.*, 2011, **133**, 10712–10715.
39 H.-J. Sun, Y. Tu, C.-L. Wang, R. M. Van Horn, C.-C. Tsai, M. J. Graham, B. Sun, B. Lotz, W.-B. Zhang and S. Z. D. Cheng, *J. Mater. Chem.*, 2011, **21**, 14240–14247.
40 C.-L. Wang, W.-B. Zhang, C.-H. Hsu, H.-J. Sun, H. R. M. Van, Y. Tu, D. V. Anokhin, D. A. Ivanov and S. Z. D. Cheng, *Soft Matter*, 2011, **7**, 6135–6143.
41 B. Eisenberg, *Acc. Chem. Res.*, 1998, **31**, 117–123.
42 J. M. Lehn, *Angew. Chem.*, 1988, **100**, 91–116.
43 G. M. Whitesides, J. P. Mathias and C. T. Seto, *Science*, 1991, **254**, 1312–1319.
44 H. Shen, K.-U. Jeong, M. Graham, S. Leng, H. Huang, B. Lotz, H. Hou, F. Harris and S. Cheng, *J. Macromol. Sci., Part B: Phys.*, 2006, **45**, 215–229.
45 H. Shen, K.-U. Jeong, H. Xiong, M. J. Graham, S. Leng, J. X. Zheng, H. Huang, M. Guo, F. W. Harris and S. Z. D. Cheng, *Soft Matter*, 2006, **2**, 232–242.
46 C. Xue, S. Jin, X. Weng, J. J. Ge, Z. Shen, H. Shen, M. J. Graham, K.-U. Jeong, H. Huang, D. Zhang, M. Guo, F. W. Harris, S. Z. D. Cheng, C. Y. Li and L. Zhu, *Chem. Mater.*, 2004, **16**, 1014–1025.
47 G. Ungar, D. Abramic, V. Percec and J. A. Heck, *Liq. Cryst.*, 1996, **21**, 73–86.
48 E. Fernandez-Megia, J. Correa, I. Rodriguez-Meizoso and R. Riguera, *Macromolecules*, 2006, **39**, 2113–2120.
49 J. Chen, S. Z. D. Cheng, S. S. Wu, B. Lotz and J.-C. Wittmann, *J. Polym. Sci., Part B: Polym. Phys.*, 1995, **33**, 1851–1855.
50 J. C. Wittmann and B. Lotz, *J. Polym. Sci., Polym. Phys. Ed.*, 1985, **23**, 205–226.
51 Y. Cao, R. M. Van Horn, H.-J. Sun, G. Zhang, C.-L. Wang, K.-U. Jeong, F. Auriemma, C. De Rosa, B. Lotz and S. Z. D. Cheng, *Macromolecules*, 2011, **44**, 3916–3923.
52 R. M. Van Horn, J. X. Zheng, H. J. Sun, M. S. Hsiao, W. B. Zhang, X. H. Dong, J. Xu, E. L. Thomas, B. Lotz and S. Z. D. Cheng, *Macromolecules*, 2010, **43**, 6113–6119.
53 S. Z. D. Cheng, Z. Wu, M. Eashoo, S. L. Hsu and F. W. Harris, *Polymer*, 1991, **32**, 1803–1810.
54 M. Eashoo, Z. Wu, A. Zhang, D. Shen, C. Tse, F. W. Harris, S. Z. D. Cheng, K. H. Gardner and B. S. Hsiao, *Macromol. Chem. Phys.*, 1994, **195**, 2207–2225.
55 U. S. Jeng, C.-H. Su, C.-J. Su, K.-F. Liao, W.-T. Chuang, Y.-H. Lai, J.-W. Chang, Y.-J. Chen, Y.-S. Huang, M.-T. Lee, K.-L. Yu, J.-M. Lin, D.-G. Liu, C.-F. Chang, C.-Y. Liu, C.-H. Chang and K.-S. Liang, *J. Appl. Crystallogr.*, 2010, **43**, 110–121.
56 S. Z. D. Cheng, *Phase Transitions in Polymers: The Role of Metastable States*, Elsevier Science, 2008.
57 R. Pardey, D. X. Shen, P. A. Gabori, F. W. Harris, S. Z. D. Cheng, J. Adduci, J. V. Facinelli and R. W. Lenz, *Macromolecules*, 1993, **26**, 3687–3697.
58 R. Pardey, S. S. Wu, J. H. Chen, F. W. Harris, S. Z. D. Cheng, A. Keller, J. Aducci, J. V. Facinelli and R. W. Lenz, *Macromolecules*, 1994, **27**, 5794–5802.
59 R. Pardey, A. Zhang, P. A. Gabori, F. W. Harris, S. Z. D. Cheng, J. Adduci, J. V. Facinelli and R. W. Lenz, *Macromolecules*, 1992, **25**, 5060–5068.
60 C. Bunn, *Trans. Faraday Soc.*, 1939, **35**, 482–491.
61 G. Ungar, *J. Phys. Chem.*, 1983, **87**, 689–695.
62 G. Ungar, *Macromolecules*, 1986, **19**, 1317–1324.
63 G. Ungar and N. Masic, *J. Phys. Chem.*, 1985, **89**, 1036–1042.
64 B. Lotz, A. J. Lovinger and R. E. Cais, *Macromolecules*, 1988, **21**, 2375–2382.
65 A. J. Lovinger, B. Lotz, D. D. Davis and F. J. Padden, *Macromolecules*, 1993, **26**, 3494–3503.
66 B. Lotz, J. C. Wittmann, R. W. cahn, P. Haasen and E. J. Kramer, in *Mater. Sci. Technol.*, VCH, Weinheim, 1993, vol. 12, pp. 79–151.
67 C. Y. Li, S. Z. D. Cheng, J. J. Ge, F. Bai, J. Z. Zhang, F. W. Harris, L.-C. Chien, D. Yan, T. He and B. Lotz, *Phys. Rev. Lett.*, 1999, **83**, 4558–4561.
68 C. Y. Li, S. Z. D. Cheng, X. Weng, J. J. Ge, F. Bai, J. Z. Zhang, B. H. Calhoun, F. W. Harris, L.-C. Chien and B. Lotz, *J. Am. Chem. Soc.*, 2001, **123**, 2462–2463.
69 J. Wang, C. Li, S. Jin, X. Weng, R. M. Van Horn, M. J. Graham, W.-B. Zhang, K.-U. Jeong, F. W. Harris, B. Lotz and S. Z. D. Cheng, *Ind. Eng. Chem. Res.*, 2010, **49**, 11936–11947.
70 V. Percec, D. A. Wilson, P. Leowanawat, C. J. Wilson, A. D. Hughes, M. S. Kaucher, D. A. Hammer, D. H. Levine, A. J. Kim, F. S. Bates, K. P. Davis, T. P. Lodge, M. L. Klein, V. R. H. De, E. Aqad, B. M. Rosen, A. O. Argintaru, M. J. Sienkowska, K. Rissanen, S. Nummelin and J. Ropponen, *Science*, 2010, **328**, 1009–1014.